Original Article

www.jmss.mui.ac.ir

Right Ventricle Functional Parameters Estimation in Arrhythmogenic Right Ventricular Dysplasia Using a Robust Shape Based Deformable Model

Mostafa Ghelich Oghli, Vahab Dehlaghi, Ali Mohammad Zadeh[1], Alireza Fallahi[2], Mohammad Pooyan[3]

Department of Biomedical Engineering, Kermanshah University of Medical Sciences, Kermanshah, Iran, [1]Department of Radiology, Shaheed Rajaei Cardiovascular, Medical and Research Center, Tehran, Iran, [2]Department of Biomedical Engineering, Hamedan University of Technology, Hamedan, Iran, [3]Department of Biomedical Engineering, Shahed University, Tehran, Iran

Submission: 01-07-2013 Accepted: 04-05-2014

ABSTRACT

Assessment of cardiac right-ventricle functions plays an essential role in diagnosis of arrhythmogenic right ventricular dysplasia (ARVD). Among clinical tests, cardiac magnetic resonance imaging (MRI) is now becoming the most valid imaging technique to diagnose ARVD. Fatty infiltration of the right ventricular free wall can be visible on cardiac MRI. Finding right-ventricle functional parameters from cardiac MRI images contains segmentation of right-ventricle in each slice of end diastole and end systole phases of cardiac cycle and calculation of end diastolic and end systolic volume and furthermore other functional parameters. The main problem of this task is the segmentation part. We used a robust method based on deformable model that uses shape information for segmentation of right-ventricle in short axis MRI images. After segmentation of right-ventricle from base to apex in end diastole and end systole phases of cardiac cycle, volume of right-ventricle in these phases calculated and then, ejection fraction calculated. We performed a quantitative evaluation of clinical cardiac parameters derived from the automatic segmentation by comparison against a manual delineation of the ventricles. The manually and automatically determined quantitative clinical parameters were statistically compared by means of linear regression. This fits a line to the data such that the root-mean-square error (RMSE) of the residuals is minimized. The results show low RMSE for Right Ventricle Ejection Fraction and Volume (≤ 0.06 for RV EF, and ≤ 10 mL for RV volume). Evaluation of segmentation results is also done by means of four statistical measures including sensitivity, specificity, similarity index and Jaccard index. The average value of similarity index is 86.87%. The Jaccard index mean value is 83.85% which shows a good accuracy of segmentation. The average of sensitivity is 93.9% and mean value of the specificity is 89.45%. These results show the reliability of proposed method in these cases that manual segmentation is inapplicable. Huge shape variety of right-ventricle led us to use a shape prior based method and this work can develop by four-dimensional processing for determining the first ventricular slices.

Key words: *Arrhythmogenic right ventricular dysplasia, deformable model, functional parameters, segmentation, shape prior*

INTRODUCTION

Arrhythmogenic right ventricular cardiomyopathy/arrhythmogenic right ventricular dysplasia (ARVC/ARVD) is an inherited disease that presents with sustained ventricular tachycardia. ARVD characterized by a total or partial replacement of myocardium, especially the right-ventricle myocardium, by fibro-adipose tissue, which may be diffuse. This kind of cardiomyopathy shows a marked dilatation with an alteration of the regional kinetic.[1,2] Although incidence and prevalence of ARVD are unknown, ARVD is recognized as a major cause of sudden death in young adolescents, and in one series it accounted for 20% of sudden deaths in all individuals younger than 35 years and 22% of sudden deaths in young athletes.[1] In early stages, the dysfunctions may be subtle and the diagnosis is quite difficult. On the contrary, in advanced stages, right ventricular (RV) enlargement may be evident as well as various clear clinical signs.[3] It is important to suspect any disorder in the early stages since sudden death can occur, especially in the subjects who present premature ventricular complexes or ventricular tachycardia originating from the RV. Diagnosis of ARVD needs a number of clinical tests, including the electrocardiogram (ECG), echocardiography, cardiac magnetic resonance imaging (MRI), and genetic testing. Like other kind of cardiac disorders, these tests are not perfect individually and their findings should be gathered to make a reliable diagnosis. Here, are some of clinical tests of ARVD description.

Address for correspondence:
Dr. Vahab Dehlaghi, Department of Biomedical Engineering, Kermanshah University of Medical Sciences, Kermanshah, Iran.
E-mail: vahabdehlaghi@yahoo.com

Electrocardiogram

About 90% of individuals with ARVD have some ECG abnormality. The most common ECG abnormality seen in ARVD is T wave inversion in leads V1-V3. However, this is a nonspecific finding,[4,5] and may be considered a normal variant in right bundle branch block.[6]

Echocardiography

Echocardiography may reveal an enlarged, hypo kinetic right-ventricle with a paper-thin RV free wall. The dilatation of the RV will cause dilatation of the tricuspid valve annulus, with subsequent tricuspid regurgitation. Paradoxical septal motion may also be present. However the echocardiography is cheaper and more access able, diagnosis of ARVD in echocardiography in early stages is a challenging task and almost impossible in many cases.[7]

Cardiac Magnetic Resonance Imaging

Cardiac MRI is a noninvasive imaging modality, which can be perfectly customized for each patient; furthermore, with the increased time and spatial resolutions, it provides perfect images for a complete overview of the right-ventricle (RV).[8] In facts, it allows an anatomic, functional and morphologic approach, so that it is possible to suspect several disorders despite the complex crescent shape of the RV. Cardiac MRI is now becoming the most valid imaging technique to diagnose ARVD.[9] Cardiac MRI can visualize the extreme thinning and akinesis of the RV free wall. However, the normal RV free wall may be about 3 mm thick, making the test less sensitive. One of the most advantages of cardiac MRI is its capability to show more details on a single image; therefore, it is possible to detect both papillary muscles and trabeculae. Those little parts are suspected to become hypertrophied in case of ARVD.[10]

Researches show that among these techniques, MRI allows the clearest visualization of the heart.[11] Because, as mentioned, MRI depicts both functional and structural abnormalities, positive MR imaging findings should be used as important additional criteria in the clinical diagnosis of ARVD. This fact can be inferred and is mentioned in texts that nowadays Cardiac MRI is the gold standard for assessing RV volume.[9] The wall motion analysis, which is very important in the early stages of ARVD, is still assessed visually so that even experienced operators can miss subtle abnormalities.[12] One of the most important and valuable findings in clinical tests of a patient with ARVD is cardiac functional parameters including right-ventricle end diastolic volume (RVEDV), right-ventricle end systolic volume (RVESV), ejection fraction (EF) and cardiac output (CO). Assessment of these parameters is now done by means of cardiac MRI and echocardiography. However, echocardiography due to its disability to visualize right-ventricle borders, especially in case of arrhythmic beating and dilated RV (present in ARVD) is not a suitable choice for assessment of cardiac functional parameters. To estimate these parameters, it is necessary to apply segmentation methods at each slice. The segmentation of end-diastolic (ED) and end-systolic (ES) images of the RV is currently performed manually in clinical routine. This long and tedious task, prone to intra- and inter-expert variability, requires about 20 min/ventricle by an expert clinician. In addition, in case of ARVD the wall motion abnormality makes the border of right-ventricle unclear and this makes the segmentation procedure more complicated. The great need for automated methods has led to the development of a wide variety of segmentation methods.[13] Most of these methods compute a pixel wise correspondence between the current image (or frame) and model distributions of photometric (intensity based) and geometric properties of the target objects. In a general view, methods can be categorized in thresholding,[14-16] pixel classification,[17-20] deformable models, Active Shape and Appearance models[21,23] and atlas based segmentation. Among these methods, deformable models have been greatly used as their flexibility, especially for this application,[24-28] either on the form of two-dimensional active contours or three-dimensional deformable surfaces. A review of papers on deformable models can be found in.[29] Despite of great advantages and wide range of researches use gradient based active contours; these types of deformable model methods are highly sensitive to the presence of noise and poor image contrast, which can lead to bad segmentation results. To overcome this drawback, some authors have incorporated robust region-based evolution criteria into active contour energy functional built from intensity statistics and homogeneity requirements.[30] Chan and Vese method[31] is one of the most important of such methods that is based on techniques of curve evolution, Mumford-Shah (MS) functional. These methods can deal with problems that mentioned in the primary deformable model methods, but they are not able to deal with occlusion problems or presence of strongly cluttered background.[30] Therefore, the integration of prior shape knowledge about the objects in the segmentation task represents a natural way to solve occlusion problems. Right-ventricle segmentation methods that are gathered in review papers,[11,32] mostly use strong prior information like atlas based methods, active shape and appearance models, electromechanical models, etc., However, using shape prior information in curve evolution equation, however a classic method is now, is not considered for segmentation of right-ventricle in cardiac MRI images. The aim of this study is performing a robust shape-based deformable model, described in[30] on cardiac MRI images of a patient with ARVD to estimate functional parameters of right-ventricle. To achieve this aim, first, right-ventricle should be segmented from cardiac MRI images. Second, volume estimation procedure should be applied to estimate right-ventricle volume in ED and ES phases. And finally, other right-ventricle functional parameters like EF and CO should be obtained by means of their formula. The following

sections of this paper describe the shape-based deformable model method, application of this method for segmentation of cardiac right-ventricle and calculation of RVEDV, RVESV and EF based on segmented areas. The validation of results is performed in final section.

METHODS

Principal Components Analysis as Shape Prior

Principal component analysis (PCA) aims at capturing the main variations of a training set while removing redundant information.[30,33] The idea is to apply the PCA not on the parametric geometric contours, but on the signed distance functions (SDFs) of these contours, which are implicit and parameter free representations. They justified this choice in two ways. First, SDFs provide a stronger tolerance than the parametric curves to slight misalignments during the alignment process of the training data since the values of neighboring pixels are highly correlated in a SDF. Second, this intrinsic contour representation also improves the shape registration process in terms of robustness, accuracy and speed. Indeed, the problem of the point-wise correspondence of contours (landmarks correspondence) is replaced by a problem of intensity correspondence on grid points which is easier to solve. For construction of this shape model binary shapes of the RV are needed. From a geometric point of view, the PCA analysis determines the best orthonormal basis $\{e_1 \ldots e_m\}$ of R^m to represent a set of n points $\{\phi_1 \ldots \phi_m\}$ in the sense of the least squares fitting vectors $\{e_i\}$ are given by the eigenvectors of the covariance matrix $\sum = \frac{1}{n} MM^T$ where M is a matrix whose column vectors are the n aligned training SDFs $\{\phi_j\}$. Vectors $\{e_i\}$ correspond to the principal variation directions of the set of n points. They are called the principal components. Moreover, the first P principal axes define a reduced p-dimensional vector space in R^m equivalent to a hyper-plane minimizing the sum of squared distances between this hyper-plane and the set of n points. It is important to note that the accuracy of the fitting of this p-dimensional hyper-plane in relation to the set of points can be measured in percentage by the formula $\beta = \sum_{k=1}^{p} \lambda_k \Big/ \sum_{k=1}^{n} \lambda_k$ where λ_k are the eigenvalues of $\sum$. Thus, it is possible to arbitrarily fix the fitting percentage β and represent the data in a sub-vector space of dimension p. In practice, only the first principal modes are necessary to model the biggest variations present in our training set. These P principal components are sorted in a matrix Wp.

Finally, the PCA can produce a new data based on the training set $\{\phi_j\}$:

$$\hat{\varphi} = \bar{\varphi} + W_p x_{PCA} \quad (1)$$

where x_{PCA} is called the vector of Eigen coefficients, the shape vector or the Eigen modes of variation. One of the most important issues in construction of PCA for cardiac right-ventricle in comparison with other data (like ellipses and brain left ventricles in[30]) is the huge shape variety in right-ventricle in terms of gray levels or structure shapes as "Figure 1" shows. Gray level intensities can also differ due to the use of different MRI scans. Fuzziness of images is another issue that can be observed on some parts of the images, mostly due to blood flow and partial volume effects, aggravated by respiration motion artifacts. This former effect is a consequence of nonzero thickness of MRI slices: In some areas, a voxel can be a mixture of several tissue types. In terms of shape, the ventricle varies over patients, over time (phase of cardiac cycle) and over the long axis.[32] Among these variations, shape variation over the position along the apex-base axis has a critical role in construction of PCA model. Because there is a large difference between apical slice images, basal slice images and mid-ventricular slice images as it can be seen in "Figure 1". Considering this fact, for construction of this shape model for cardiac right-ventricle, 30 binary shapes of the RV, containing mid-ventricular slices and 30 binary shapes of the RV, containing apical and basal slices, obtained by manually segmenting the RV on N cardiac MRI, are used. Hence, we have two PCA models that are apical and basal principal components and mid-ventricular principal components as it can be seen in "Figure 2".

Segmentation Model

Energy Function

Three force terms is used for curve evolution in the shape prior based segmentation method described in[30] containing shape term, region term, and boundary term. These terms are put together with this formula:

$$F = \beta_s F_{shape}(C, x_{PCA}, x_T) + \beta_b F_{boundary}(C) + \beta_r F_{region}(x_{PCA}, x_T, u_{in}, u_{out}) \quad (2)$$

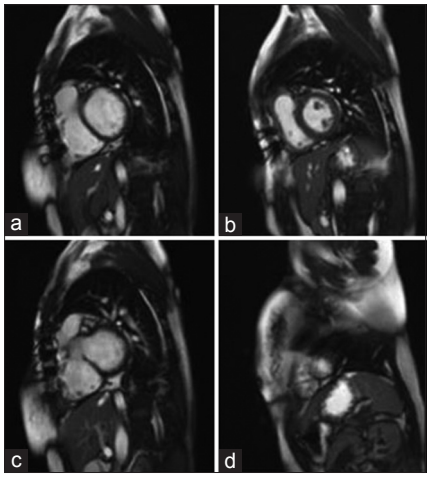

Figure 1: Various shapes of RV in cardiac MRI images (a and b) Mid-ventricular slices, (c) Apical slice, (d) Basal slice

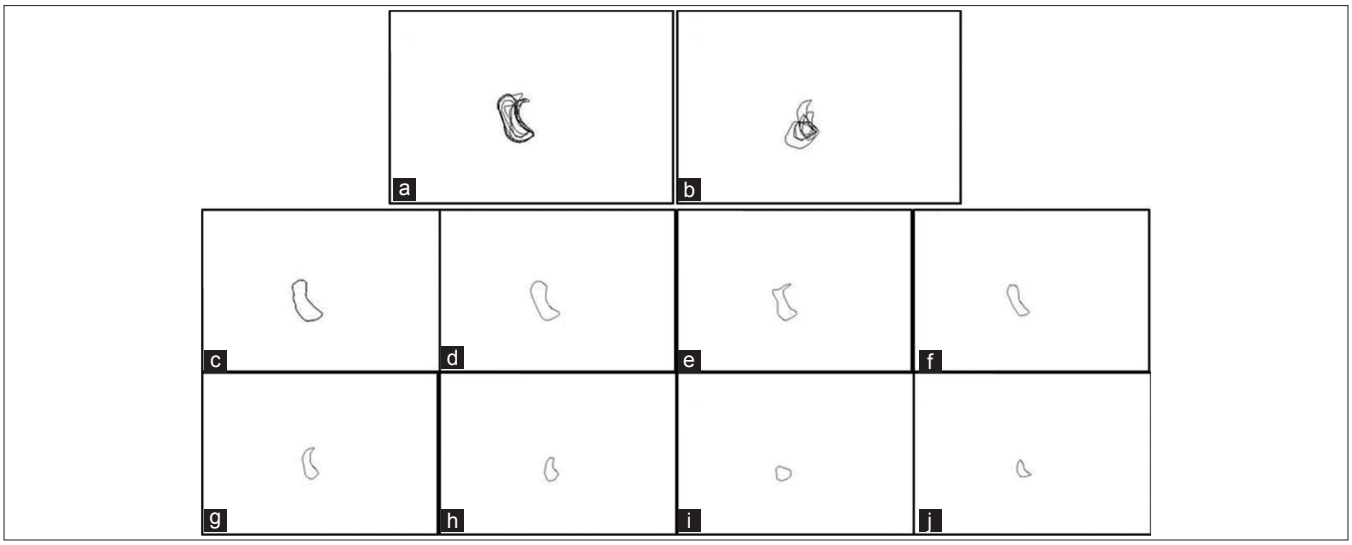

Figure 2: Representing principal component analysis for (a) Mid-ventricular slices of cardiac right-ventricle, (b) Apical and basal slices of cardiac right-ventricle (c-f) Sample binary mid-ventricular right ventricular (RV) contours (g-j) Sample apical and basal binary RV contours

where,

$$F_{\text{shape}} = \oint \hat{\varphi}^2(x_{\text{PCA}} + h_{x_T}(C_q))\left|C'(q)\right|dq, \tag{3}$$

$$F_{\text{boundary}} = \int_0^1 g\left(\left|\nabla I(C(q))\right|\right)\left|C'(q)\right|dq, \tag{4}$$

$$F_{\text{region}} = \int_{\Omega_{\text{in}}(x_{\text{PCA}},x_T)}\left(\left|I-u_{\text{in}}\right|^2 + \mu\left|\nabla u_{\text{in}}\right|^2\right)d\Omega + \int_{\Omega_{\text{out}}(x_{\text{PCA}},x_T)}\left(\left|I-u_{\text{out}}\right|^2 + \mu\left|\nabla u_{\text{out}}\right|^2\right)d\Omega \tag{5}$$

where

- C and $C(q)$ is the active contour,
- I is the original image,
- ∇ stands for gradient,
- $\hat{\varphi}$ is the shape function of the object of interest by the PCA,
- x_{PCA} is the vector of PCA Eigen coefficients,
- h_{x_T} is an element of a group of geometric transformations parameterized by x_T (the vector of parameters),
- g is an edge detection function,
- Ω_{in} and Ω_{out} are the inside and outside regions of the zero level set of $\hat{\varphi}$,
- u_{in} and u_{out} are smooth approximations of the original image and,
- $\beta_b, \beta_s, \beta_r, \mu$ are arbitrary positive constants that balance the contributions of the boundary, shape and region terms. The proposed functional F is an extension of the work of[34] where the shape model of Leventon *et al*.[33] and the MS functional[35] are integrated.

The Shape Term

F_{shape} depends on the active contour C, the vector x_{PCA} of PCA Eigen coefficients and the vector x_T of geometric transformations. This function evaluates the shape difference between the contour C and the zero level set of the shape function $\hat{\varphi}$ provided by the PCA. To give an interpretation of F_{shape} authors assumed that:

$$\hat{\varphi}^2(x_{\text{PCA}} + h_{x_T}(C_q)) = \hat{\varphi}^2(x_{\text{PCA}},(C_q)) \approx \left|\hat{C}(p_{\min}) - C(q)\right|^2 \tag{6}$$

where $|.|$ stands for Euclidean norm. "Figure 3" illustrates the function $\hat{\varphi}$ and $\hat{C}_{X_{\text{PCA}}}(p_{\min})$.

In practice, the point $\hat{C}(p_{\min})$ is not computed. It corresponds to the closest point of $C(q)$ on the zero level set of $\hat{\varphi}$ and we used it to illustrate the shape function at point $C(q)$. Indeed, the shape function $\hat{\varphi}^2(x_{\text{PCA}} + h_{x_T}(C_q))$ is equal to the distance $\left|\hat{C}(p_{\min}) - C(q)\right|^2$, that is, the value of the level set-based function $\hat{\varphi}^2$ at the point $C(q)$. Finally, F_{shape} is obtained by integrating $\hat{\varphi}^2$ along the active contour, which defines the shape similarity measure equivalent to the sum of square differences. The minimization of F_{shape} allows us to increase the similarity between the active contour and the shape model. The functional is minimized using the calculus of variations and the gradient descent method which provide three flows acting on the curve C, the vector of Eigen coefficients x_{PCA} and the vector of geometric transformations x_T. Each of three flows can be analyzed by fixing the two others. F_{shape} w.r.t the curve C (classical geodesic flow), F_{shape} w.r.t vector of Eigen coefficients x_{PCA} and F_{shape} w.r.t vector of geometric transformation x_T. Analysis of F_{shape} by means of these three flows can be expressed in a variational level set formulation as presented in[34,36] because the level set approach of these methods can be used to prove the existence of solution minimizing our energy functional in the space of functions

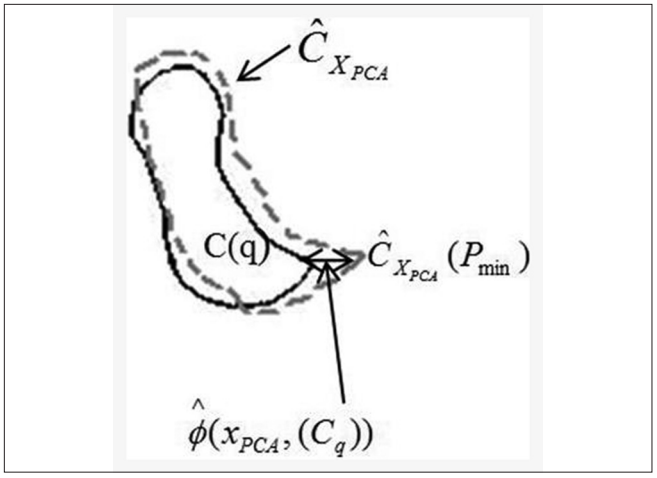

Figure 3: Illustration of the function $\hat{\varphi}(X_{PCA},(C_q))$: the square shape function is approximately equal to the square Euclidean distance between the point $C(q)$ and the closest point $\hat{C}_{X_{PCA}}(P_{min})$ on the zero level set $\hat{C}_{X_{PCA}}$ of $\hat{\varphi}(X_{PCA})$

with bounded variation. The level set formulation of the shape functional from Eq. 3 is:

$$F_{\text{shape}}=\int_{\Omega}\hat{\varphi}^2(x_{\text{PCA}},h_{x_{\text{T}}}(x))\left|\nabla\phi\right|\delta(\phi)d\Omega, \tag{7}$$

where φ is a level set function embedding the active contour C, $\delta(.)$ is the Dirac function and $\delta(\varphi)$ is the contour measure on $\{\varphi=0\}$. Coarea formulation[37] proves that the level set formulation of F_{shape} is equivalent to the geometric formulation (Eq. 3). The level set formulations of prementioned flows are:

$$\begin{cases}\partial_t\phi(t,x)=\left(\hat{\varphi}^2\kappa-\left\langle\nabla\hat{\varphi}^2,\dfrac{\nabla\phi}{|\nabla\phi|}\right\rangle\right)\delta(\phi)\\ \phi(0,x)=\phi_0(x),\text{in }\Omega\\ \dfrac{\nabla(\phi)}{|\nabla\phi|}\partial_N\phi=0\text{ on }\partial\Omega\end{cases} \tag{8}$$

$$\begin{cases}d_t x_{\text{PCA}}(t)=-2\int_{\Omega}\hat{\varphi}\nabla_{x_{\text{PCA}}}\hat{\varphi}\left|\nabla\phi\right|\delta(\phi)\,d\Omega\\ in\,]0,\infty[\times\Omega_{\text{PCA}}\\ x_{\text{PCA}}(t=0)=x_{\text{PCA}_0}\text{ in }\Omega_{\text{PCA}}\end{cases} \tag{9}$$

$$\begin{cases}d_t x_{\text{T}}(t)=-2\int_{\Omega}\hat{\varphi}\left\langle\nabla\hat{\varphi},\nabla x_{\text{T}}h_{x_{\text{T}}}\right\rangle\left|\nabla\phi\right|\delta(\phi)\,d\Omega\\ in\,]0,\infty[\times\Omega_{\text{T}}\\ x_{\text{T}}(t=0)=x_{\text{T}_0}\text{ in }\Omega_{\text{T}}\end{cases} \tag{10}$$

In segmentation model described in,[30] the flows given by the Eq. 8-10 are simultaneously used to constraint the active contour to get a shape of interest whatever the position of the active contour in the image. There is a solution for solving these equations that will be discussed in section 2-3.

The region term

The authors of[30] have defined a functional to drive the shape model toward a homogeneous intensity region with the shape of interest. It has been proved in[30] that if our objects of interest are supposed to have a smooth intensity surface then the MS model is the most adapted model to segment these objects. Since the MS method applied on the active contour will extract globally homogeneous regions[30] and our objective is to capture an object belonging to a given shape space then the best solution is to apply the MS-based force on the shape prior. Indeed, this new force will globally drive the shape prior towards a homogeneous intensity region with the shape of interest. Because of using PCA as shape prior, the MS method is modified:

$$\begin{aligned}F_{\text{region}}=&\oint_{\hat{C}(x_{\text{PCA}},x_{\text{T}})}ds+\int_{\Omega_{\text{in}}(x_{\text{PCA}},x_{\text{T}})}\left(\left|I-u_{\text{in}}\right|^2+\mu\left|\nabla u_{in}\right|^2\right)d\Omega\\&+\int_{\Omega_{\text{out}}(x_{\text{PCA}},x_{\text{T}})}\left(\left|I-u_{\text{out}}\right|^2+\mu\left|\nabla u_{\text{out}}\right|^2\right)d\Omega\end{aligned} \tag{11}$$

where the curve $\hat{c}$ is the zero level set of the shape function $\hat{\varphi}$ extracted from the PCA process. The function $\hat{\varphi}$ defines an image partitioned into two regions Ω_{in} and Ω_{out}, representing respectively the object and the background, whose common boundary is $\hat{C}$:

$$\begin{cases}\Omega_{\text{in}}(x_{\text{PCA}},x_{\text{T}})=\left\{x\in\Omega\left|\hat{\varphi}(x,x_{\text{PCA}},x_{\text{T}})>0\right.\right\},\\ \Omega_{\text{out}}(x_{\text{PCA}},x_T)=\left\{x\in\Omega\left|\hat{\varphi}(x,x_{PCA},x_T)<0\right.\right\},\\ \hat{C}_{\_\_}(x_{\text{PCA}},x_{\text{T}})=\left\{x\in\Omega\left|\hat{\varphi}(x,x_{\text{PCA}},x_{\text{T}})=0\right.\right\}.\end{cases} \tag{12}$$

As it mentioned in Eq. 5, we have not considered the smoothing term, $\oint_{\hat{C}}ds$, since shapes generated by the PCA are smooth enough. The functional F_{region} can be re-written with the shape function $\hat{\varphi}$:

$$\begin{aligned}F_{\text{region}}=&\int_{\Omega}\Theta_{\text{in}}H(\hat{\varphi}(x_{\text{PCA}},x_{\text{T}}))\,d\Omega\\&+\int_{\Omega}\Theta_{\text{out}}H(-\hat{\varphi}(x_{\text{PCA}},x_{\text{T}}))\,d\Omega\end{aligned} \tag{13}$$

where $H(.)$ is the Heaviside function, $\Theta_{\text{r}}=\left|I-u_{\text{r}}\right|^2+\mu\left|\nabla u_{\text{r}}\right|^2$ and r = in or out. For minimization of MS function the gradient descent method for $x_{\text{PCA}},x_{\text{T}}$ and solving the Euler-Lagrange equations for $u_{\text{in}},u_{\text{out}}$ are needed:

$$\begin{cases}d_t x_{\text{PCA}}(t)=\int_{\Omega}(\Theta_{\text{in}}-\Theta_{\text{out}})\nabla_{x_{PCA}}\hat{\varphi}\delta(\phi)\,d\Omega\\ in\,]0,\infty[\times\Omega_{\text{PCA}}\\ x_{\text{PCA}}(t=0)=x_{\text{PCA}_0}\text{ in }\Omega_{\text{PCA}}\end{cases} \tag{14}$$

$$\begin{cases}d_t x_{\text{T}}(t)=\int_{\Omega}(\Theta_{\text{in}}-\Theta_{\text{out}})\left\langle\nabla\hat{\varphi},\nabla x_{\text{T}}h_{x_{\text{T}}}\right\rangle\delta(\phi)\,d\Omega\\ \text{in }]0,\infty[\times\Omega_{\text{T}}\\ x_{\text{T}}(t=0)=x_{\text{T}_0}\text{ in }\Omega_{\text{T}}\end{cases} \tag{15}$$

$$\begin{cases} \partial_t u_{in}(t,x) = u_{in} - I - \mu\Delta u_{in} \\ \text{in }]0,\infty[\times \{\hat{\varphi} > 0\} \\ u_{in}(0,x) = I \text{ in} \{\hat{\varphi} > 0\} \\ \partial_t u_{out}(t,x) = u_{out} - I - \mu\Delta u_{out} \\ \text{in }]0,\infty[\times \{\hat{\varphi} < 0\} \\ u_{in}(0,x) = I \qquad in \{\hat{\varphi} < 0\} \end{cases} \tag{16}$$

As it mentioned in pervious section, there is a solution for solving these equations that will be discussed in section 2-3.

The Boundary Term

As it can be seen in "Figure 4," using shape and region force leads the curve to a predefined shape and homogeneous region and these forces cannot handle local structure variations.

The model has not captured the local edge variations since it only deals with global shape variations provided by the PCA model. The model should be able to capture the local variations around the global shape; hence, adding local criteria to our energy functional is needed. We will consider for this purpose the classic geodesic active contour given by F_{boundary}. The formulation of F_{boundary} is mentioned in Eq. 4 and propose an energy function that leads our curve to the boundaries of RV.

A Numerical Solution

The authors in[30] obtained a system of coupled evolution equations whose steady-state solution gives the minimum of *F*, which means the solution of the segmentation problem. The functional *F* is expressed in the Eulerian/level set framework as follows:

$$F = \int_\Omega f(x, x_{PCA}, x_T)\left|\nabla\phi\right|\delta(\phi)\,d\Omega + \beta_r \int_\Omega \left(\Theta_{in} H(\hat{\varphi}(x_{PCA}, x_T)) + \Theta_{out} H(-\hat{\varphi})\right) d\Omega \tag{17}$$

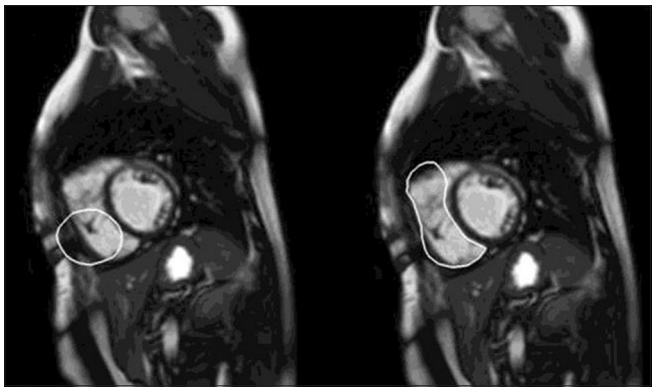

Figure 4: Examples of not perfect segmentation results of using active contour in absence of boundary force and under region and shape force

where

$$f(x, x_{PCA}, x_T) = \beta_s \hat{\varphi}^2(x_{PCA}, h_{x_T}(x)) + \beta_b g\left(\left|\nabla I(x)\right|\right) \tag{18}$$

And the evolution equations minimizing *F* are:

$$\begin{cases} \partial_t \phi(t,x) = \left(f\kappa - \left\langle \nabla f, \dfrac{\nabla\phi}{|\nabla\phi|} \right\rangle \right) \delta(\phi) \\ \phi(0,x) = \phi_0(x), \text{in } \Omega \\ \dfrac{\delta(\phi)}{|\nabla\phi|} \partial_N \phi = 0 \text{ on } \partial\Omega \end{cases} \tag{19}$$

$$\begin{cases} d_t x_{PCA}(t) \\ \quad = -\int_\Omega \nabla_{x_{PCA}} \hat{\varphi} \left(2\beta_s \hat{\varphi} |\nabla\phi| \delta(\phi) + \beta_r (\Theta_{in} - \Theta_{out}) \delta(\hat{\phi}) \right) d\Omega \\ \text{in }]0,\infty[\times \Omega_{PCA} \\ x_{PCA}(t=0) = x_{PCA_0} \text{ in } \Omega_{PCA} \end{cases} \tag{20}$$

$$\begin{cases} d_t x_T(t) = -2\int_\Omega \left\langle \nabla\hat{\varphi}, \nabla x_T h_{x_T} \right\rangle \left(\begin{matrix} 2\beta_s \hat{\varphi} |\nabla\phi| \delta(\phi) \\ + \beta_r (\Theta_{in} - \Theta_{out}) \delta(\hat{\phi}) \end{matrix} \right) d\Omega \\ \text{in }]0,\infty[\times \Omega_T \\ x_T(t=0) = x_{T_0} \text{ in } \Omega_T \end{cases} \tag{21}$$

$$\begin{cases} \partial_t u_{in}(t,x) = u_{in} - I - \mu\Delta u_{in} \\ \text{in }]0,\infty[\times \{\hat{\varphi} > 0\} \\ u_{in}(0,x) = I \text{ in} \{\hat{\varphi} > 0\} \\ \partial_t u_{out}(t,x) = u_{out} - I - \mu\Delta u_{out} \\ \text{in }]0,\infty[\times \{\hat{\varphi} < 0\} \\ u_{in}(0,x) = I \text{ in} \{\hat{\varphi} < 0\} \end{cases} \tag{22}$$

These evolution equations are numerically solved by an iterative procedure until convergence is reached. This procedure stages are as follows:

- Computation of the shape function $\hat{\varphi}(x_{PCA}, x_T)$ using Eq. 1 and performing the rigid and affine transformations (scaling, rotation, translations and shearing) with the B-spline interpolation method[38]
- Calculation of the gradient $\nabla\hat{\varphi}$ using a central difference scheme. The term $\nabla_{x_{PCA}}\hat{\varphi}$ is given by the eigenvectors of the PCA model
- Discretization of terms $|\nabla\varphi|$ and $\left\langle \nabla f, \dfrac{\nabla\varphi}{|\nabla\varphi|} \right\rangle$ with the Osher–Sethian numerical scheme.[39] Computation of the curvature with central difference schemes
- Functions u_{in} and u_{out} are computed in $\{\hat{\varphi} > 0\}$ and $\{\hat{\varphi} < 0\}$ with the method proposed in[30]
- Computation of Eq. 19-22

- Level set function evolution at each iteration by means of the fast marching method that is presented in.[40]

This method robustly segments right-ventricle in cardiac short axis MRI images for patients with ARVD from base to apex. This can be seen in "Figure 5." The result of using two groups of principal components for basal and apical slices and mid-ventricular slices in implementation of this method can be seen in first and second row of "Figure 6."

Calculation of Functional Parameters

A number of parameters are used to evaluate ventricular (LV and RV) function. Volumetric measurements of the ventricles are performed on images obtained at ED and ES. ED and ES are determined visually as the cardiac phases that yield the maximum (end-diastolic volume [EDV]) and minimum (end-systolic volume [ESV]) RV volumes. These two volumes can then be used to determine the EF. The EF, defined as the proportion of blood ejected with each right ventricular (RV) contraction and mathematically is calculated by dividing subtraction of ESV from the EDV by the EDV. The advent of advanced tomographic techniques, such as cardiovascular magnetic resonance (CMR), has allowed for the accurate quantification of ventricular volumes. This method relies on Simpson's rule, which simply divides a large volume into smaller, more accurately measurable segments that are then summed. Compared with the geometric assumptions that are made with the modified Simpson's rule, a technique generally used with modalities such as echocardiography and radioscintigraphy, volumetric measurements using Simpson's rule in CMR are more accurate and have superior intra- and inter-observer reproducibility. On the basis of Simpson's rule, the segmented pixels of all images are counted and multiplied by their voxel size and the voxel size is defined as pixel_spacing_x * pixel_spacing_y * slice_thickness. Hence, volume of the right-ventricle is determined through contiguous short axis slice models by:

$$V = T\sum_{i=1}^{n} A_i \tag{23}$$

In this equation V denotes the RV volume, T denotes the slice thickness and A_i denotes the area of the RV cavity for the i^{th} slice. After applying segmentation method to the ED and ES phases of cardiac cycle, and measuring right-ventricle volume, EF is calculated by prementioned formula:

$$EF = \frac{\text{EDV} - \text{ESV}}{\text{EDV}} \times 100 \tag{24}$$

RESULT

This algorithm is tested on 30 cardiac short axis MRI images for patients with ARVD in size of 347 × 510 and obtained acceptable results. The implementation of this method is done using MATLAB 7.12.0.635 (R2011a) with License Number: 161052. Natick, Massachusetts, U.S.A.. Figure 7 shows a visual comparison between our method and manual segmentation. Anterior wall and lateral-basal wall mis-segmentation in manual segmentation of some slices is observable in this "figure 7".

To validate the segmentation results and qualitative comparison, we compared obtained results with manual segmentation performed by a senior radiologist. Table 1 shows cardiac functional parameters of 10 numbers of

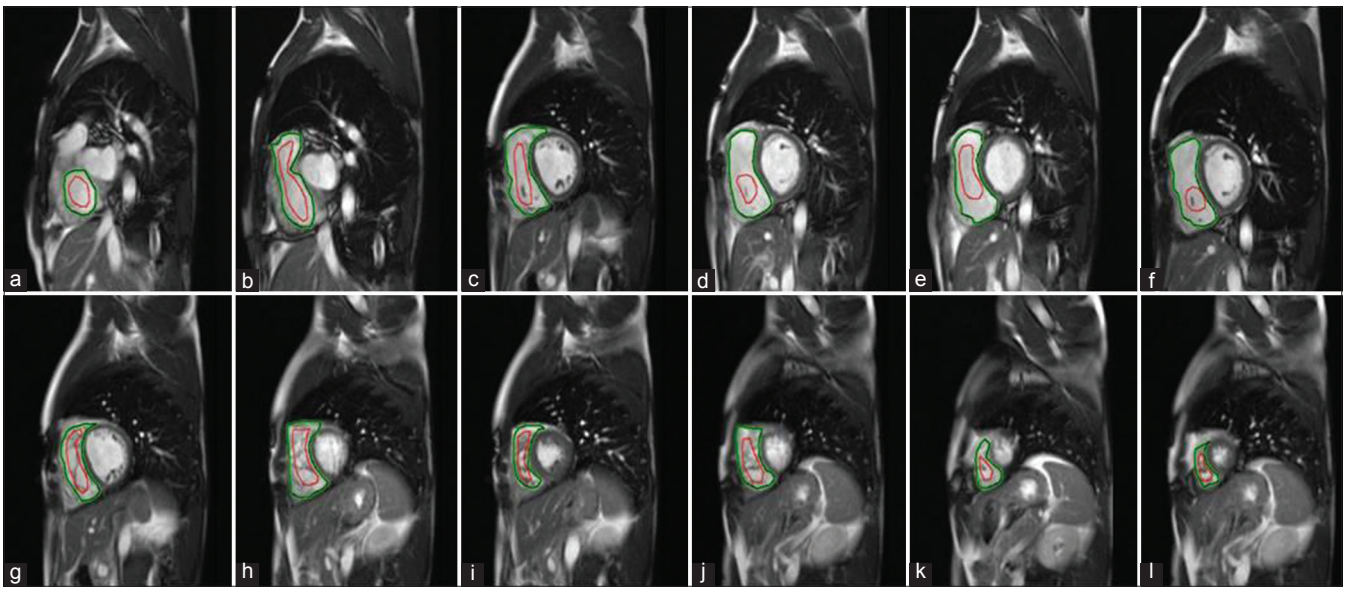

Figure 5: Segmentation of right ventricular from (a) base to (l) apex for a 34-year-old patient with arrhythmogenic right ventricular dysplasia. Red contour: Initial contour; green contour: Segmentation result

tested data that are obtained by segmentation of RV by introduced method. We performed a quantitative evaluation of clinical cardiac parameters derived from the automatic segmentation by comparison against a manual delineation of the ventricles performed on two-dimensional short-axis slices by a radiologist with experience in cardiac MR imaging. The manual delineation was a regular clinical quantification performed at the Shahid Rajaie Hospital a Philips EasyVision workstation, on patients with suspected ARVD. The manually and automatically determined quantitative clinical parameters were statistically compared by means of linear regression. This fits a line to the data such that the root-mean-square error (RMSE) of the residuals is minimized $\left(RMSE = \sqrt{SSR/n-2}\right)$, where *SSR* is the sum of squared residuals, and *n* is the number of data points. The comparative quantitative results for RV EF, and right-ventricle volume are shown in "Figure 7." These plots indicate how well the automatic segmentation (X axis) can predict the volumes and EFs obtained using the manual expert segmentation (Y axis). The linear regression has a low RMSE (≤0.06 for RV EF, and ≤10 mL for RV volume). Evaluation of segmentation results is also done by means of four statistical measures contain sensitivity, specificity, similarity index (SI) and Jaccard index (JI). If *M* denote segmented region by an expert radiologist and *A* denote segmented region by means of our proposed algorithm, then these four statistical measures will define simply.

- Sensitivity relates to the test's ability to identify a condition correctly and it is defined by formula:

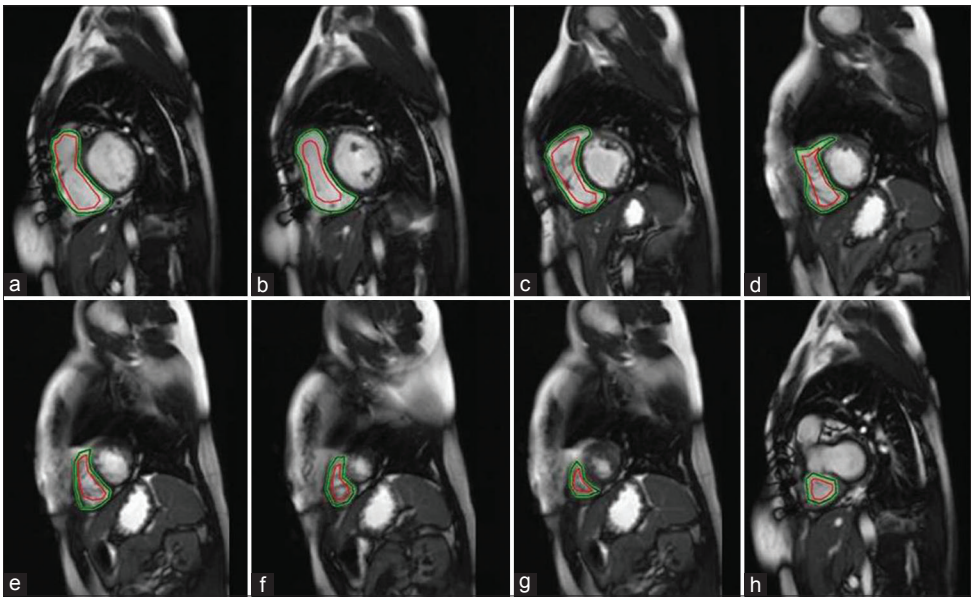

Figure 6: Result of segmentation of right-ventricle in cine magnetic resonance imaging for patients with arrhythmogenic right ventricular dysplasia in (a-d) Mid-ventricular slices and (e-h) Apical and basal slices. These two groups used two principal components. Red contour: Initial contour; green contour: Segmentation result

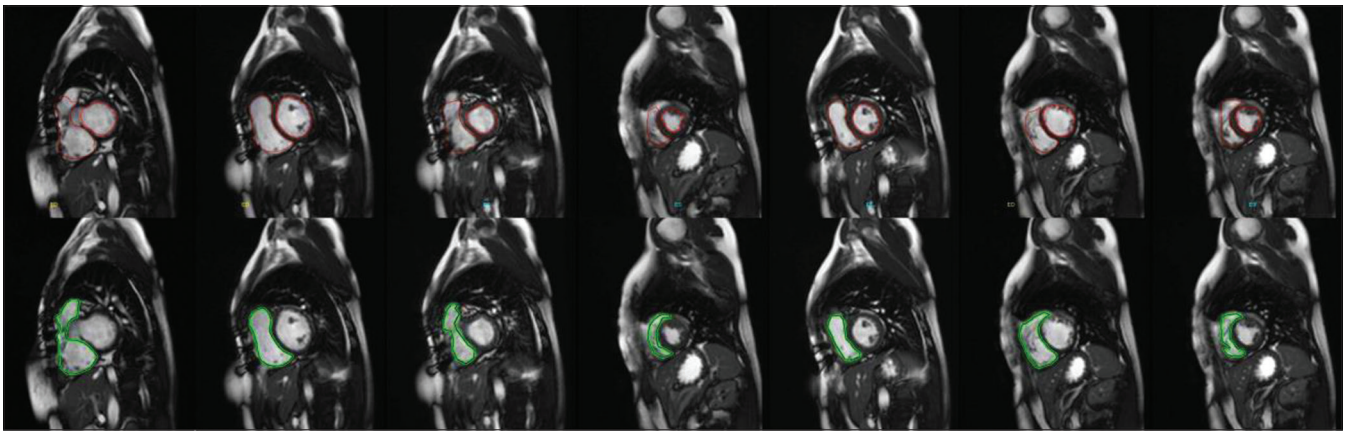

Figure 7: Comparison of proposed algorithm segmentation results with manual segmentation. Top row: Manual segmentation by an expert radiologist (mis-segmentation of anterior wall and lateral-basal wall in some slices is obvious). Bottom row: Proposed algorithm segmentation results

$$T_p = \frac{N_{T_p}}{N_M} \times 100\% \quad (25)$$

Where N_{T_p} is the number of true positive and N_M is the cardinality of *M*.

- Specificity relates to the test's ability to exclude a condition correctly and it is defined by formula:

$$S_E = 100 - F_p; F_p = \frac{N_{F_p}}{N_A} \times 100\% \quad (26)$$

Where N_A is the cardinality of *A* and N_{F_p} is the number of false positive;

- SI: $$S_i = \frac{2N_{T_p}}{N_M + N_A} \times 100\% \quad (27)$$

- JI: $$S_i = \frac{2N_{T_p}}{N_M + N_A} \times 100\% \quad (28)$$

Table 2 shows evaluation of the segmentation of RV on 30 datasets. Results show that this algorithm can robustly segments RV on MR cardiac images.

DISCUSSION

Cardiac MRI due to its capabilities in imaging a complete overview of the right-ventricle is becoming a more and more important helpful means in diagnosing ARVC/ARVD. ARVD is a progressive disease leading to RV failure and several dysfunctions. Right-ventricle functional parameters play an essential role in diagnosis of ARVD. Assessment of these parameters needs segmentation of right-ventricle at each slice of cardiac MRI images. Unclear border of right-ventricle in Cardiac MRI images of patients with ARVD is a huge difficulty in the way of segmentation methods and that is because of existence of cardiac arrhythmic beating in these patients. Level set techniques are by now well-known and used in many tools, in fact it is impossible to segment complex shapes as RV without making geometrical assumptions. But using only contour information leads the curve to undesired results. So regards to complexities of right-ventricle segmentation, region and shape information of right-ventricle is added to the equation assumptions in this paper. Right-ventricle segmentation methods mostly use strong prior information such as atlas based methods, active shape and appearance models, electromechanical models etc., However using shape prior information in curve evolution equation; however, is now a classic method, is not considered for segmentation of right-ventricle in cardiac MRI images. Our aim was using a shape based deformable model for segmentation of right-ventricle in cardiac short axis MRI images for patients with ARVD. Shape prior information was added to the equations by means of PCA. PCA aims at capturing the main variations of a training set while removing redundant information. However, there was a problem in preparing shape prior information by PCA and that was the huge shape variety of right-ventricle that comes from position of MRI slices along the apex-base axis. For fixing this problem, principal components

Table 1: ESV and EDV volumes and calculated EF of some patients

Parameter number	EDV (ml)	ESV (ml)	EF (%)	EF (%) manual
1	224.4	170.5	24.019	23.890
2	218.5	165.5	51.716	58.342
3	256.3	173.4	32.345	37.212
4	209.4	121.1	42.168	40.016
5	172.2	94.0	45.412	44.997
6	200.1	115.2	42.429	42
7	194.0	125.7	35.206	38.001
8	220.1	107.5	51.158	50.151
9	165.8	63.2	61.881	65.435
10	188.5	55.6	70.503	73.331

ESV – End-systolic volume; EDV – End-diastolic volume; EF – Ejection fraction

Table 2: Evaluation of segmentation results by means of four measures contain SI, JI, SE and SP for which an expert radiologist segmentation was available

Patient number	Volume metric (%)			
	SI	JI	SE	SP
1	85.5978	80.3763	89.1969	85.2435
2	87.2959	88.4740	97.0071	91.5367
3	90.3595	79.9001	89.2175	87.9648
4	87.3468	78.1490	90.4044	95.6853
5	84.1068	84.1002	97.2664	94.7292
6	84.6101	91.4642	94.9833	89.7468
7	86.5344	83.3248	97.3334	88.0938
8	86.4733	84.4840	95.3341	93.4030
9	84.5857	79.3732	90.7154	84.8979
10	87.5159	90.0843	90.1394	91.6327
11	90.5563	83.7325	96.8215	86.6643
12	86.3067	85.3934	89.3369	87.6588
13	86.4372	79.3165	98.8120	86.6543
14	80.8457	86.7216	96.7926	91.2698
15	84.8414	84.8155	94.2274	86.2611
16	83.1088	78.4804	92.7765	85.2048
17	85.9285	83.3829	94.6246	91.1860
18	88.4816	81.3725	110.7461	87.5733
19	91.2752	83.6679	92.1866	90.4779
20	92.0458	82.1927	84.8214	87.8380
21	86.6827	82.4414	102.5270	90.1373
22	86.1135	78.9851	95.8702	79.6515
23	89.2990	81.8945	89.4557	90.8637
24	88.3824	86.3628	106.1084	95.9982
25	89.1527	90.3732	95.5698	92.9854
26	89.1892	78.4619	94.2604	92.5103
27	82.8651	92.9674	88.7930	88.2530
28	88.5230	89.4769	87.3289	89.8097
29	86.7537	83.9109	83.7411	90.0437
30	84.8813	81.9851	90.6031	89.4967
Standard deviation	2.5818	4.1311	5.8215	3.5217
Average result	86.8699	83.8555	93.9	89.4490

SI – Similarity index; JI – Jaccard index; SE – Sensitivity; SP – Specificity

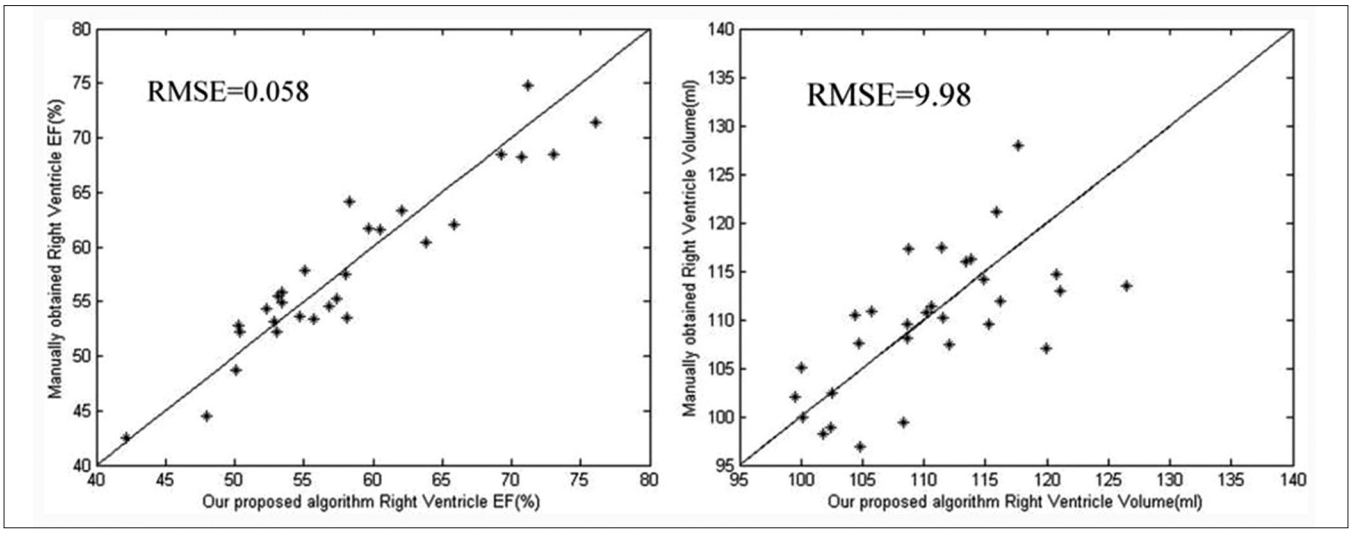

Figure 8: Right-ventricle ejection fraction (left plot) and volume (right plot), determined by the human expert and by the automatic segmentation for 30 exams. The root mean square error is expressed in the same units as the ejection fraction and volume

provided in two groups that was basal and apical slices and mid-ventricular slices. Choosing between these two shape information terms was performed manually. Three force terms was used for curve evolution in the proposed method containing shape term, region term and boundary term that are gathered in an equation called energy function. Each term of this equation was weighted by a positive constant. And all parts of energy function were solved by numerical solutions. The main goal of numerical solution is minimizing energy function that leads the curve to a homogenous region (regards to region term), borders of right-ventricle (regards to boundary term) and a predefined shape of right-ventricle (prepared by PCA regards to shape term). Future researches can develop this work by defining a parameter for choosing shape information terms or four-dimensional processing of short axis cardiac MRI images for determining the first ventricular slices.

ACKNOWLEDGMENTS

This paper is prepared from thesis No. 92208 that is done in Kermanshah University of Medical Sciences as a Ms thesis.

REFERENCES

1. Thiene G, Nava A, Corrado D, Rossi L, Pennelli N. Right ventricular cardiomyopathy and sudden death in young people. N Engl J Med 1988;318:129-33.
2. Daliento L, Turrini P, Nava A, Rizzoli G, Angelini A, Buja G, *et al*. Arrhythmogenic right ventricular cardiomyopathy in young versus adult patients: Similarities and differences. J Am Coll Cardiol 1995;25:655-64.
3. Fontaine G, Gallais Y, Fornes P, Hébert JL, Frank R. Arrhythmogenic right ventricular dysplasia/cardiomyopathy. Anesthesiology 2001;95:250-4.
4. Keshtkar A, Seyedarabi H, and Sheikhzadeh P. Discriminant analysis between myocardial infarction patients and healthy subjects using Wavelet Transformed signal averaged electrocardiogram and probabilistic neural network. Journal of Medical Signals and Sensors, 2013;3:225:31.
5. Safdarian N, Dabanloo NJ, Matini SA, Nasrabadi AM. Rule-based Method for Extent and Localization of Myocardial Infarction by Extracted Features of ECG Signals using Body Surface Potential Map Data. Journal of medical signals and sensors 2013;3:129.
6. Piccini JP, Nasir K, Bomma C, Tandri H, Dalal D, Tichnell C, *et al*. Electrocardiographic findings over time in arrhythmogenic right ventricular dysplasia/cardiomyopathy. Am J Cardiol 2005;96:122-6.
7. Yoerger DM, Marcus F, Sherrill D, Calkins H, Towbin JA, Zareba W, *et al*. Echocardiographic findings in patients meeting task force criteria for arrhythmogenic right ventricular dysplasia: New insights from the multidisciplinary study of right ventricular dysplasia. J Am Coll Cardiol 2005;45:860-5.
8. Bluemke DA, Krupinski EA, Ovitt T, Gear K, Unger E, Axel L, *et al*. MR Imaging of arrhythmogenic right ventricular cardiomyopathy: Morphologic findings and interobserver reliability. Cardiology 2003;99:153-62.
9. Lemmo M, Azarine A, Tarroni G, Corsi C, Lamberti C. (2010, September). Estimation of right ventricular volume, quantitative assessment of wall motion and trabeculae mass in arrhythmogenic right ventricular dysplasia. Comput Cardiol 2010, IEEE; 2010.
10. Spreeuwers LJ, Bangma SJ, Meerwaldt RJ, Vonken EJ, Breeuwer M. Detection of trabeculae and papillary muscles in cardiac MR images. Comput Cardiol 2005;32:415-8.
11. Petitjean C, Dacher JN. A review of segmentation methods in short axis cardiac MR images. Med Image Anal 2011;15:169-84.
12. Indik JH, Wichter T, Gear K, Dallas WJ, Marcus FI. Quantitative assessment of angiographic right ventricular wall motion in arrhythmogenic right ventricular dysplasia/cardiomyopathy (ARVD/C). J Cardiovasc Electrophysiol 2008;19:39-45.
13. Frangi AF, Niessen WJ, Viergever MA. Three-dimensional modeling for functional analysis of cardiac images: A review. IEEE Trans Med Imaging 2001;20:2-25.
14. Goshtasby A, Turner DA. Segmentation of cardiac cine MR images for extraction of right and left ventricular chambers. IEEE Trans Med Imaging 1995;14:56-64.
15. Lee HY, Codella NC, Cham MD, Weinsaft JW, Wang Y. Automatic left ventricle segmentation using iterative thresholding and an active contour model with adaptation on short-axis cardiac MRI. Biomedical Engineering, IEEE Transactions 2010;57:905-13.
16. Codella NC, Lee HY, Fieno DS, Chen DW, Hurtado-Rua S, Kochar M, *et al*. Improved Left Ventricular Mass Quantification With Partial

Voxel Interpolation *In Vivo* and Necropsy Validation of a Novel Cardiac MRI Segmentation Algorithm. Circulation: Cardiovascular Imaging, 2012;5:137-46.
17. Pednekar A, Kurkure U, Muthupillai R, Flamm S, Kakadiaris IA. Automated left ventricular segmentation in cardiac MRI. IEEE Trans Biomed Eng 2006;53:1425-8.
18. Lynch M, Ghita O, Whelan PF. Automatic segmentation of the left ventricle cavity and myocardium in MRI data. Comput Biol Med 2006;36:389-407.
19. Kurkure U, Pednekar A, Muthupillai R, Flamm SD, Kakadiaris Ast IA. Localization and segmentation of left ventricle in cardiac cine-MR images. IEEE Trans Biomed Eng 2009;56:1360-70.
20. Cousty J, Najman L, Couprie M, Clément-Guinaudeau S, Goissen T, Garot J. Segmentation of 4D cardiac MRI: Automated method based on spatio-temporal watershed cuts. Image and Vision Computing 2010;28:1229-43.
21. Tobon-Gomez C, Sukno FM, Butakoff C, Huguet M, Frangi AF. Automatic training and reliability estimation for 3D ASM applied to cardiac MRI segmentation. Physics in medicine and biology 2012;57: 4155.
22. Andreopoulos A, Tsotsos JK. Efficient and generalizable statistical models of shape and appearance for analysis of cardiac MRI. Medical Image Analysis 2008;12:335-57.
23. Grosgeorge D, Petitjean C, Caudron J, Fares J, Dacher JN. Automatic cardiac ventricle segmentation in MR images: A validation study. International journal of computer assisted radiology and surgery 2011;6:573-81.
24. El Berbari R, Bloch I, Redheuil A, Angelini E, Mousseaux E, Frouin F, *et al*. An automated myocardial segmentation in cardiac MRI. Conf Proc IEEE Eng Med Biol Soc 2007;2007:4508-11.
25. Xu C, Pham DL, Prince JL. Medical image segmentation using deformable models. Handbook of Medical Imaging. Medical Image Processing and Analysis. Vol. 2. May 2000, United State: SPIE Press; p. 129-74.
26. Paragios N. A variational approach for the segmentation of the left ventricle in cardiac image analysis. International Journal of Computer Vision 2002;50:345-62.
27. Chakraborty A, Staib LH, Duncan JS. Deformable boundary finding in medical images by integrating gradient and region information. IEEE Trans Med Imaging 1996;15:859-70.
28. Sun H, Frangi AF, Wang H, Sukno FM, Tobon-Gomez C, Yushkevich PA. (2010). Automatic cardiac MRI segmentation using a biventricular deformable medial model. In Medical Image Computing and Computer-Assisted Intervention–MICCAI 2010 (pp. 468-475). Springer Berlin Heidelberg.
29. Singh A, Goldgof D, Terzopoulos D. Deformable Models in Medical Image Analysis. Los Alamitos, CA, USA: IEEE Computer Society Press; 1998.
30. Bresson X, Vandergheynst P, Thiran JP. A variational model for object segmentation using boundary information and shape prior driven by the Mumford-Shah functional. Int J Comput Vis 2006;68:145-62.
31. Chan TF, Vese LA. Active contours without edges. IEEE Trans Image Process 2001;10:266-77.
32. Alfakih K, Reid S, Jones T, Sivananthan M. Assessment of ventricular function and mass by cardiac magnetic resonance imaging. Eur Radiol 2004;14:1813-22.
33. Leventon M, Grimson W, and Faugeras O. Statistical shape influence in geodesic active contours. In: IEEE International Conference of Computer Vision and Pattern Recognition; 2000. p. 316-23.
34. Chen Y, Tagare HD, Thiruvenkadam S, Huang F, Wilson D, Gopinath KS, *et al*. Using prior shapes in geometric active contours in a variational framework. Int J Comput Vis 2002;50:315-28.
35. Mumford D, Shah J. Optimal approximations of piecewise smooth functions and associated variational problems. Commun Pure Appl Math 1989;42:577-685.
36. Zhao H, Chan T, Merriman B, Osher S. A variational level set approach to multiphase motion. J Comput Phys 1996;127:179-95.
37. Evans LC, Gariepy RF. Measure Theory and Fine Properties of Functions, Studies in Advanced Mathematics. United State: CRC Press; 1992.
38. Unser M. Splines: A perfect fit for signal and image processing. IEEE Signal Process Mag 1999;16:22-38.
39. Osher S, Sethian JA. Fronts propagating with curvature dependent speed: Algorithms based on Hamilton-Jacobi formulations. J Comput Phys 1988;79:2-49.
40. Adalsteinsson D, Sethian J. A fast level set method for propagating interfaces. J Comput Phys 1995;118:269-77.

How to cite this article: Oghli GM, Dehlaghi V, Zadeh AM, Fallahi A, Pooyan M. Right Ventricle Functional Parameters Estimation in Arrhythmogenic Right Ventricular Dysplasia Using a Robust Shape Based Deformable Model. J Med Sign Sence 2014;4:211-22.

Source of Support: This paper is prepared from thesis No. 92208 that is done in Kermanshah University of Medical Sciences as a Ms thesis, **Conflict of Interest:** None declared

BIOGRAPHIES

Mostafa Ghelich Oghli, PhD student of Biomedical Engineering in Isfahan University of Medical Sciences, Isfahan, Iran. He received a B.Sc. degree in Biomedical Engineering from Department of Biomedical Engineering, Shahed University, Tehran, Iran, and he received his M.Sc. degree in Biomedical Engineering from Department of Biomedical Engineering, Kermanshah University of Medical Sciences, Kermanshah, Iran. His research interest is Medical Image Analysis, especially Cardiac MRI Image Analysis.

E-mail: m.g31_mesu@yahoo.com

Dr. Vahab Dehlaghi was born on April 30, 1973 in Sahneh, Kermanshah, IRAN. He received a B.Sc. in Mechanical Engineering in 1995 from Department of Mechanical Engineering, Iran University of Science and Technology, Tehran, Iran and his M.Sc. and PhD degrees in Biomedical Engineering in 1998 and 2007 from Sharif University of Technology and Amirkabir University of Technology respectively. He has a Post-Doctoral research fellow from Biomechanics laboratory, Biomedical Engineering Department, Erasmus MC, Rotterdam, Netherlands. Since 2007, He has been assistant professor in Biomedical Engineering Department, at Kermanshah University of Medical Sciences, Kermanshah, Iran. His research area is CFD in biological systems and cardiovascular hemodynamics.

E-mail: vahabdehlaghi@yahoo.com

Dr. Ali Mohammad Zadeh was born in 1976. He graduated MD from Shaheed Beheshti University in 2003 and he graduated degree in Radiology from Shaheed Beheshti University in 2010. Since 2010 he has been assistant professor of Iran University of Medical Sciences. His research interests are in the field of Radiology, Doppler Ultra Sonography, CT Angiography and Interventional Radiology.

E-mail: mralimohammadzadeh@yahoo.com

Alireza Fallahi, lecturer in Biomedical Engineering Department, Hamedan University of Technology, Hamedan, Iran. He received a B.sc. degree in Electrical Engineering from Tabriz University at 2007 and M.Sc. degree in Biomedical Engineering from Shahed University at 2010. His research interests are Medical Signal and Image Processing and fMRI.

E-mail: ali.r.fallahi@gmail.com

Dr. Mohammad Pooyan, Associate professor in Biomedical Engineering Department, Shahed University, Tehran, Iran. He received his B.Sc. and M.Sc. degree in Electronics Engineering from Shiraz University and Tarbiat Modares University respectively. He has a PhD in Biomedical Engineering from Tarbiat Modares University. His current research interests are in the field of Medical Image Processing, Cardiac Signal Analysis, Bioinstruments and Microprocessors.

E-mail: pooyan@shahed.ac.ir